Investigation of transient PVC dynamics in a strongly swirled spray flame using high speed planar laser imaging of SnO 2 microparticles

Guillaume Vignat, Daniel Durox, Antoine Renaud, Théa Lancien, Ronan Vicquelin, Sébastien Candel

Version of Record: https://www.sciencedirect.com/science/article/pii/S0010218020305009
Manuscript_978899d80afe7c6265197c8c566e5723

Investigation of transient PVC dynamics in a strongly swirled spray flame using high speed planar laser imaging of SnO_2 microparticles

Guillaume Vignat[a,*], Daniel Durox[a], Antoine Renaud[a], Théa Lancien[a], Ronan Vicquelin[a], Sébastien Candel[a]

[a] *Laboratoire EM2C, CNRS, CentraleSupélec, Université Paris-Saclay, 3, rue Joliot Curie, 91192 Gif-sur-Yvette, France*

Abstract

The Precessing Vortex Core (PVC) dynamics is investigated in a laboratory scale swirl stabilized spray combustor. This helical structure commonly found in swirling flows used to stabilize flames in many combustion systems has a notable impact on the structure of the flow, spray and flame formed by the injector unit. The dynamics of the PVC is examined by combining laser sheet illumination of flame front tracers filmed with a high speed camera, Proper Orthogonal mode Decomposition (POD) and wavelet analysis. In distinction with most applications of laser sheet illumination, in which the flow is seeded with oil droplets that vanish at a relatively low temperature when crossing the flame front, the present implementation relies on micronic tin oxide (SnO_2) particles that vanish at much higher temperatures. This is well suited to flows where fresh reactants are already at high temperature or where hot gases are recirculated as is the case in most swirling injection configurations. A first set of experiments carried out with stagnation point premixed flames is used to determine the temperature ($T_v \approx 1770$ K) at which the tin dioxide vanish and to identify the chemical reaction that controls this process. Because the light scattered by the solid particles is quite intense, the method can be used at very high repetition rates. It is then applied at a 100 kHz frame rate to a swirling injection configuration in a situation where the flame is well stabilized and the combustor does not exhibit thermoacoustic instabilities. It is found that the PVC takes the form of a double helix with brief intermittent switching to a single, followed by a triple helicoidal geometry. The POD-wavelet analysis indicates that these moments correspond to flashback events that randomly occur and during which the PVC characteristics change for a few milliseconds at a time. In a second set of experiments the chamber length is augmented giving rise to a combustion instability coupled by a longitudinal acoustic mode at a frequency that is an order of magnitude lower than the PVC frequency. The planar slices of the flame reveal a large cyclic motion of the lower edge of the flame in the inner recirculation zone. It is found that the PVC is modulated both in amplitude and frequency, the modulating frequency corresponding to that of the thermoacoustic oscillation. The double helix PVC is also observed to vanish in a random manner.

Keywords:
Swirl spray flame; Precessing Vortex Core; Planar laser sheet illumination in flames; High repetition rate diagnostics; Intermittent structures; Thermoacoustic instabilities; Tracer of the flame front

*Corresponding author:
Email address: guillaume.vignat@centralesupelec.fr
(Guillaume Vignat)

1. Introduction

Swirling flows are commonly used in many combustion systems to stabilize the flame at a distance from the combustor walls by recirculation of hot gases around the axis of the burner and in outer regions adjacent to the stream of fresh reactants. The corresponding flames are relatively compact and fairly stable. To assist engineering design, it is important to characterize their structure and dynamical behavior and identify mechanisms that control their sensitivity to perturbations and determine the position of the flame edge in the injector near field to avoid hot spots, flashback, extinctions and combustion instabilities. It is logical to examine the behavior of these flames in representative configurations and use spatially resolved imaging tools that allow high frame rate operation to examine these flows. The present investigation illustrates one possible method consisting in illuminating the flame with a continuous planar laser sheet and seeding the flow with tracers which disappear in the flame front. Images acquired at up to 100 kHz allow to identify the structure of the precessing vortex core (PVC) in a swirling flow, examine its transient dynamics and accompanying flame motion and characterize modulations of the PVC induced by combustion instabilities.

It is worth at this point briefly reviewing optical techniques that might allow high rate imaging and could be used to investigate practical swirling reactive flows. One possibility would be to use fast imaging of the chemiluminescent emission. The light signal emitted by flames is generally not of a sufficient level for exposure durations corresponding to frame rates of the order of ten kHz or more. Using current imaging technology, visualizations of light emission from conventional hydrocarbon flames at atmospheric pressure may be achieved up to a sampling rate of about 6 kHz [1–4]. Density gradients can be visualized using backlighting and full-field interferometry at very high repetition rates: 200 kHz in [5]. However, these techniques only give access to line-of-sight integrated images, which complicate the signal interpretation and the extraction of the flame front dynamics. Another powerful method is planar laser induced fluorescence (PLIF) of chemical species like OH. This radical appears near the end of the reactive zone and it persists in the burnt gases thus marking the flame front. Recently developed high repetition rate lasers allow a temporal resolution of the motion of the OH layer at rates of the order of 10 kHz. OH-PLIF imaging, widely used in combustion, has been applied to the study of the dynamics of swirled flames [6–9]. This method requires the use of pulsed, tunable lasers, and at high repetition rate the energy per pulse is fairly low, limiting the signal to noise ratio in the recorded images. Additionally, in high pressure applications, higher collisional quenching rates further reduce the fluorescence signal. Simpler flame front visualization methods based on tomography have been used for many years. The first objective of this article is to explore this standard path by specifically considering issues raised by the tracer's characteristics and by examining the possible use of particles featuring relatively high vanishing temperatures.

The availability of fairly powerful continuous lasers allowed the first developments of planar laser tomography aimed at visualizing flame fronts. The technique consists in seeding the reactive flow with a tracer which either appears or vanishes when crossing the flame front. In 1980, Boyer [10] suggested using micronic oil droplets to seed the reactive flow. These tracers mark the flame front boundary on the fresh stream side [11], and the isotherm where these droplets vanish corresponds to approximately 570 K, with some small variations depending on the type of oil [3, 12, 13]. This technique has been used extensively to analyze the dynamics of simple flame fronts [14] and time tracking was achieved in the 1990s with pulsed lasers operating at high repetition rates such as copper vapor lasers delivering light pulses at a rate of a few kilohertz in combination with fast film cameras [15]. One advantage of flame tomography is its straightforward combination with PIV measurements to simultaneously determine the position of the flame front, its velocity and the velocity of the stream of fresh gases [13, 16, 17]. Upton et al. [18] expanded on this method by performing a 3D reconstruction of a turbulent premixed jet flame. The position of the flame front was determined by the disappearance of oil droplets used as seeders. Ebi and Clemens [3] also performed a 3D reconstruction in a combustor featuring a lean-premixed swirling flame with a higher acquisition rate of 5 kHz. Simultaneous stereoscopic PIV was used to determine the three components of the velocity in the fresh stream. Although the terms "laser tomography" and "flame tomography" have been used in many early works to designate this flame visualization method, in recent years, the use of these terms has evolved and they now refer to "computed tomography" techniques. To avoid confusion, the terms "laser sheet illumination" and "planar illumination" will be used in the remainder of this article.

In many applications where combustion is confined, the temperature of the fresh reactants can be higher than 570 K and in those cases the tracer oil droplets would be vaporized before reaching the flame front. This is

the case, for example, in many systems operated above atmospheric pressure, in certain swirling flames with strong recirculation typical of gas turbines, in industrial furnaces equipped with heat recovery systems, in automobile engines just before ignition. It is then no longer possible to use oil droplets. This observation led to exploring seeding with titanium tetrachloride ($TiCl_4$) injected into the fresh stream in liquid form. $TiCl_4$ reacts with the water vapor formed during combustion to produce micronic particles of TiO_2 [19]. A laser can then be used to visualize the reaction zone: its light is scattered by the titanium oxide particles conveyed in the burnt stream, thus marking the location of hot combustion products. This technique provides high quality planar images, but has the drawback of producing hydrochloric acid during the reaction, which limits its practical application. The possible use of other solid tracers that vanish when crossing a flame front was reviewed early on by Dumont and Borghi [12] who quote temperatures at which particles disappear, either by sublimation, or through liquefaction. Some of these solid tracers are notably toxic while others modify the flame color, such as phosphorus pentaoxide P_2O_5, molybdenum trioxide MoO_3, zinc sulfide ZnS, or antimony trioxide Sb_2O_3. Among the particles used to seed reactive flows, titanium dioxide TiO_2 and zirconium dioxide ZrO_2 are often favored by experimenters, because they are resistant to high temperatures ($> 2300\,\mathrm{K}$), but they are generally not suitable for tracing the reaction fronts of hydrocarbon-air flames. According to [12] tin dioxide SnO_2 particles appear particularly interesting in cases where the fresh stream is brought to a high temperature of a few hundred degrees. The particle size of tin dioxide is in the micronic range and the distribution of particle sizes is relatively narrow. Dumont and Borghi [12] suggest that SnO_2 particles vanish at a temperature of 1820 K, while the PubChem database [20] reports that its melting temperature is around 1900 K and its boiling temperature is in the range 2070−2170 K.

It is clear that tin dioxide tracers merit some attention and its use is explored in what follows with the aim of examining strongly swirled flame dynamics. These flames are stabilized in the vicinity of a spray swirled injector of the type used to study the circular ignition ("light round") in a transparent annular chamber (MICCA-Spray) representative of an annular combustor [2, 4, 21]. The swirl number measured at the injector outlet is relatively high (0.68) [2], imposing a strong recirculation of burnt combustion products on the axis. This high level of swirl makes it likely that one or two precessing vortex structures exist in the flow. In the case considered in what follows experiments indicate that there are two helical structures for the Precessing Vortex Core (PVC), a feature that is also retrieved in a large eddy simulation and that will be studied in some detail using the SnO_2 planar illumination technique.

It is worth at this point briefly reviewing the literature on PVCs in swirling flows and swirl-stabilized flames. This topic is discussed in isothermal conditions in the review on vortex breakdown [22], and in flames in the reviews [23, 24]. In combustion applications, swirling injectors are used to aerodynamically stabilize the flame at a distance from the combustor walls. This is possible because, for a sufficiently high level of swirl, the flow undergoes vortex breakdown, a phenomenon whereby an inner recirculation zone forms on the centerline of the flow. As the swirl number is increased, a spiraling vortex structure appears in the vicinity of the inner shear layer as a result of a super-critical Hopf bifurcation [25–27]. This structure established between the inner recirculation zone and the main flow [8, 25, 27–30] precesses in the same direction as the flow but is winding in the opposite direction [25]. The PVC is a global mode of instability [26, 31, 32]. It creates a fully synchronized motion in the entirety of the flow, at a frequency that increases linearly with the flow rate [22, 23, 33] and is also related to the swirl number S [22, 34]. Manoharan et al. [27] have recently shown that this dependency is of the form $f_{PVC} \propto S - S_c$ where S_c is a critical swirl number. Naturally, the amplitude of this helical disturbance decays downstream of the injector, and vanishes after one to two nozzle outlet diameters [28, 30].

It is generally possible to associate an azimuthal wavenumber m to the PVC that reflects the angular periodicity of this coherent structure. A single helix structure corresponds to an azimuthal wavenumber $m = 1$ and is observed in many studies of swirling injectors [8, 28–30, 35–40]. In some instances, more complex structures associated with higher azimuthal wavenumbers have been observed. In laminar flows in solid body rotation with a flat axial velocity profile, Billant et al. and Liang and Maxworthy [25, 41] report observing intertwined periodic helical structures associated with higher wavenumbers $m = 2$ and $m = 3$. Liang and Maxworthy [25] also observe weak structures associated with even higher wavenumbers ($m = 4, 5$), and show that the precession frequency of the PVC, f_{PVC}, is strongly tied to the rotation rate of the flow Ω by $m\Omega = f_{PVC}$. Vanierschot et al. [42] studied specifically single- and double-helix PVCs in a radial swirler with a central bluff-body, using time-resolved PIV, POD and linear stability analysis (LSA). They concluded in particular that the frequency of the double-helix is not necessarily the double of that of the single helix-structure.

Vigueras-Zuniga et al. [43] present some striking images of a flame stabilized inside a double helix PVC ($m = 2$). Structures of this type have been reported in other experimental investigations of swirled flames [8, 9, 23, 44].

The effect of a flame on a preexisting PVC is complex: in some cases, the PVC is suppressed by the flame [28, 36, 37], while in others it persists and its strength may be enhanced [23, 35, 38]. In other conditions, these two outcomes are observed depending on the operating conditions and associated flame shapes [8, 39]. The injection of fuel on the centerline of the injector can also affect the PVC [40, 45]. Yin and Stöhr [9] used multi-resolution POD (MRPOD) to study the PVC in a bistable swirled premixed flame. They found that the PVC observed when the flame was stabilized in its "M"-shape was strongly damped and essentially vanished when the flame was established as a "V"-shape in the inner shear layer of the IRZ. In this regard, Terhaar et al. [39] performed an interesting parametric study in a premixed confined swirled burner. By modifying operating conditions such as fuel type, equivalence ratio, preheating temperature, steam dilution and injection bulk velocity, they were able to stabilize the flame in four distinct shapes. Depending on the flame shape, the existence and frequency of the PVC were varied. By using a local LSA on the mean flow field, measured by PIV (velocity) and quantitative light sheet determination of the density, these authors were able to retrieve the frequency and location of the PVC. Their analysis indicates that the relationship between PVC, rotation rate and flame shape is complex, and that the backflow velocity and density gradients in the inner shear layer between the IRZ and the jet play a major role.

The present study comprises four parts. In the first, the objective is to obtain the temperature value T_v at which particles of SnO_2 vanish. This is accomplished by making use of a set of atmospheric pressure hydrocarbon-air flames operating at different equivalence ratios. In the second part, the dynamics of the swirling spray flame is examined. The air used in this combustion process is seeded with fine tin dioxide particles. It is shown that SnO_2 microparticles allow to detect the flame front, but also to identify the PVC. In the third part, POD image processing and wavelet analysis are employed to analyze the dynamics of this helical structure. It is found that the PVC forms a double helix structure, that switches to a single and then triple helical structures during short intermittent flashback events. Finally, in Section 5, the combustion chamber is lengthened into a configuration giving rise to combustion instabilities coupled by a longitudinal acoustic mode. The shape of the flame in the IRZ is determined for different phase instants during the thermoacoustic cycle. It is also demonstrated that the PVC is modulated by the combustion oscillation, both in terms of intensity and precession frequency.

2. Measurement of the temperature at which tin dioxide particles vanish

Tin dioxide is a material of high technical importance to a number of industries. Its application as a flame front tracer is however not well documented. The aim of the present section is to see if SnO_2 can be used in this application, and to determine the temperature at which it vanishes. This is accomplished by examining methane-air laminar flames formed in a stagnation point flow in a well controlled configuration used to obtain images of the particles trajectories with planar laser illumination. By varying the equivalence ratio, it is possible to change the temperature at the end of combustion in the flame zone and deduce from images whether the solid particles disappear or not when crossing the flame front. For each equivalence ratio, the temperature profile in the flame is determined using a 1D simulation with a detailed chemistry. This gives access to the characteristic temperature at which the SnO_2 particles vanish in a typical hydrocarbon-air flame at atmospheric pressure.

2.1. Experimental set up

A diagram of the stagnation point burner used for this measurement is shown in Fig. 1. This system has a flat cooled copper wall 90 mm in diameter and 10 mm thick, placed perpendicular to the burner axis. The burner outlet diameter is 22 mm. The distance from the plate to the burner outlet is also 22 mm. Methane and air are premixed prior to entering the burner. Bronkhorst ELFlow mass flow meters are used to adjust the mixture mass flow rates. Their relative precision is 0.2% in the range of interest. A flow of $0.3\,\mathrm{L\,min^{-1}}$ of water circulates in a coil to cool the copper plate. A K-type thermocouple is placed in the center of the plate. During the experiments, the temperature of the plate stays between 318 and 324 K. Without flame, but with air flow, the temperature is 285 K. A vertical laser sheet about 50 mm high traverses the flow from the left of the burner to the right in an axial plane. This sheet is formed by a continuous laser operating at 532 nm with a power of 1 W. The optical assembly includes a cylindrical lens with a short focal length and a spherical lens with 300 mm focal length. Micronic SnO_2 particles are injected into the air stream, well upstream of the burner

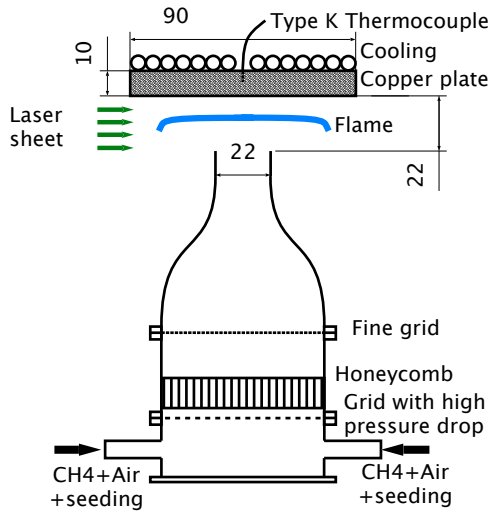

Figure 1: Schematic diagram of the burner used for the study of the temperature T_v at which tin dioxide particles vanish. A plate is placed 22 mm above and parallel to the burner nozzle, such that a flat, stagnation point laminar flame is formed. The plate is water cooled to maintain a constant temperature at all equivalence ratios.

Table 1: Operating conditions and temperatures at the end of combustion.

Test	1	2	3	4	5	6
U_b (m s^{-1})	0.778	0.777	0.776	0.775	0.774	0.773
ϕ	0.705	0.691	0.677	0.662	0.648	0.634
T_c (K)	1842	1819	1795	1770	1745	1721

using a cyclonic system. The number distribution for the diameter of the tin dioxide particles is given by the manufacturer as follows: 10% < 0.39 µm; 50% < 1.04 µm; 90% < 2.86 µm. The average particle diameter is d_{10} = 1.38 µm. The tests are carried out for a fixed air flow rate and the equivalence ratio of the mixture is set by adjusting the methane flow rate. The mixture velocity at the outlet of the burner varies between 0.773 and 0.778 m s^{-1} and the equivalence ratio ϕ between 0.634 and 0.705. Under these conditions, the flame is detached from the burner and established in the central part. It is nearly flat and parallel to the cooled plate.

2.2. Results

The test conditions are indicated in Tab. 1. The bulk velocity at the burner outlet (U_b) slightly varies because the methane flow rate is changed but this does not affect the results. The maximum temperature reached during combustion T_c is determined with the 1D flame simulation code "Agath", developed in house at EM2C laboratory, using a skeletal kinetic scheme GRI-Mech for methane-air combustion [46]. In these counterflow simulations, the uniform bulk velocity and the temperature of the fresh stream of 293 K are set at the burner exit while null velocities and 322 K are prescribed at the plate.

Typical flame images are displayed in Fig. 2. The flow is seeded with SnO_2 microparticles, which are illuminated by a laser sheet. The flame stabilizes at the point where the laminar burning velocity is equal to the axial component of the flow velocity. At the top left the flame is furthest away from the plate because this configuration corresponds to the highest value of the equivalence ratio and correspondingly to the greatest laminar burning velocity. By decreasing the equivalence ratio, from left to right and from top to bottom, the burning velocity decreases and the flame approaches the plate since the flow velocity at the nozzle has hardly changed. For equivalence ratios between 0.705 and 0.677, the tin dioxide particles completely vanish when crossing the flame front. In the image at the bottom left (ϕ = 0.662), some particles succeed to cross the flame front, but there is a notable difference in brightness between the particle traces in the fresh stream and in the burnt gases. In the last two images all particles cross the flame front and remain visible in the hot stream. According to Tab. 1, one may consider that below 1745 K the particles do not vanish. At 1770 K some of the particles vanish, but some do not, most probably those featuring the largest initial diameters. One may conclude from these data that the tin dioxide particles mark an isotherm that approximately corresponds to a temperature of 1770 K for typical hydrocarbon-air flames at atmospheric pressures. This is slightly lower than the temperature indicated in [12] and much lower than the temperature quoted in the PubChem database [20].

2.3. Discussion

It is first useful to note that there is some debate as to the melting point of SnO_2. A value of 1903 K is often quoted [20, 47, 48]. This contrasts with the experiments of [49] who suggest that the melting point is higher than 2370 K from experiments conducted at partial pressures of O_2 closer to those found in combustion applications. In any case, both these temperatures notably exceed the vanishing temperature obtained in the present work with a flat flame.

Thin films of SnO_2 are quite often formed using chemical vapor deposition (CVD). One of the first application of CVD for SnO_2 has been published by Marley and MacAvoy [50]. Their process involves heating very pure SnO_2 at 1923 K to vaporize this compound before crystallization at a lower temperature further down the

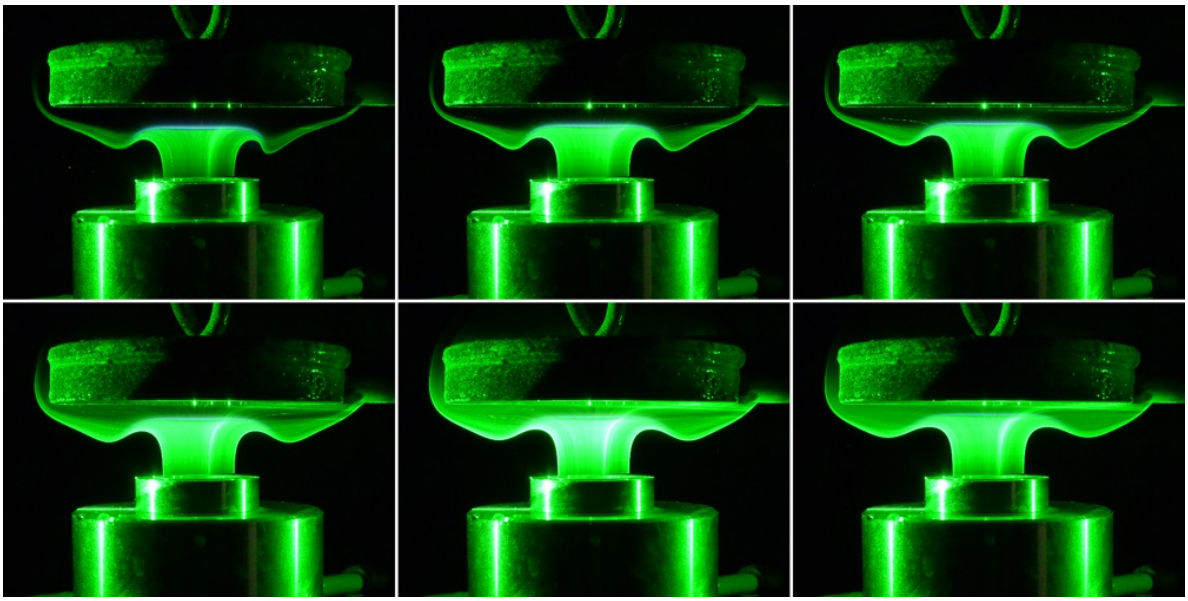

Figure 2: Planar flame visualizations obtained by seeding the reactive flow with tin dioxide particles. The flame can be distinguished by a slight blue color. The green laser sheet illuminates the particles. A co-current annular nozzle surrounds the burner, but is not operated in this study. From left to right, and from top to bottom, the equivalence ratio is: 0.705, 0.691, 0.677, 0.662, 0.648 and 0.634.

furnace. The authors note that the chemical composition of the gases in the furnace is of great importance to the process. In an atmosphere devoid of oxygen, in addition to evaporation, solid SnO_2 may be decomposed as

$$SnO_2(s) \rightleftharpoons SnO(g) + \frac{1}{2}O_2(g) \tag{1}$$

Articles published later on confirmed that this reaction is an important process for the disappearance of SnO_2 in a high temperature environment [47, 48, 51]. Of specific interest to the present application as a flame tracer is the partial pressure of O_2 at equilibrium determined experimentally in [51] for this reaction:

$$\log\left(p^{eq}_{O_2}\right) = 3.72 - \frac{20050}{T} \tag{2}$$

This was determined in a vacuum chamber using a Langmuir experimental apparatus. In this correlation, $p^{eq}_{O_2}$ is given in Pa. At atmospheric pressure and for $T = 1770\,\mathrm{K}$, one finds a volume fraction of O_2 at equilibrium of $X^{eq}_{O_2} = 2.5 \times 10^{-3}$, which is significantly smaller than the O_2 mass fraction in the burnt gases of the lean premixed flames used in the previous section. This indicates that the dissociation reaction (1) is not important in the stagnation point flames shown in Fig. 2.

In contrast, Galazka et al. [49] suggest that, in the presence of gaseous CO and CO_2, another reaction may prevail:

$$SnO_2(s) + CO(g) \rightleftharpoons SnO(g) + CO_2(g) \tag{3}$$

For an ambient gas made of CO_2 at 1 bar, they calculate for this endothermic reaction an equilibrium temperature of $T_{eq} = 1759\,\mathrm{K}$. This is quite close to the vanishing temperature determined using the flat flame apparatus, and one may tentatively conclude that this process controls the disappearance of SnO_2 particles in hydrocarbon-air flames.

This analysis allows to identify which type of configurations may benefit from using SnO_2 as flame tracers. First it is worth underlining that the 1770 K disappearance temperature only applies to hydrocarbon-air flames at ambient pressure. Several parameters may affect the exact value of that temperature, such as the chemical composition of the reactive mixture, ambient pressure... Second, one may also ask whether the temperature is influenced by the particle size. Two batches of SnO_2 particles from different suppliers have been tested, indicating that the size of SnO_2 particles does not affect the disappearance temperature for particles smaller than 2.5 µm. To tentatively conclude, SnO_2 should be used to trace flame fronts when oil droplet seeding would be ineffective because of premature disappearance. For hydrocarbon-air flames, SnO_2 can reliably be used if the burnt gas temperature is significantly higher than 1770 K.

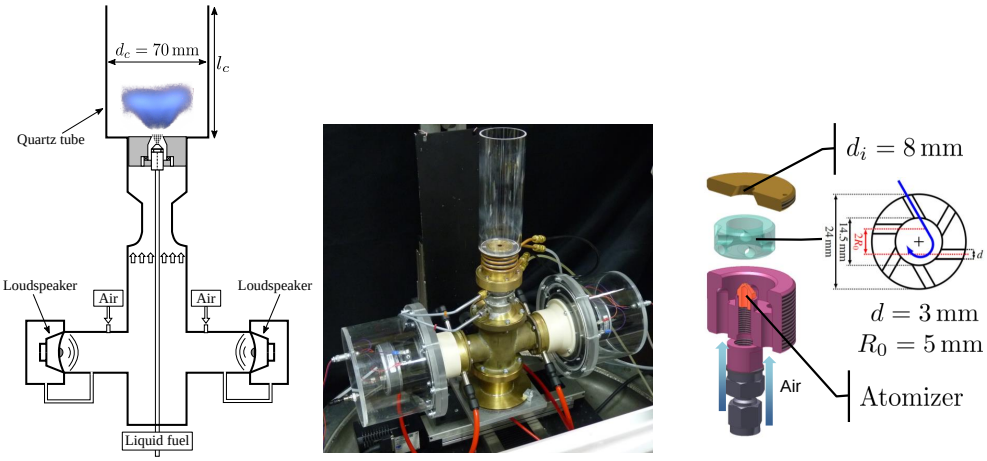

Figure 3: Left, schematic view and photography of the experimental rig with its cylindrical quartz flame tube 200 mm long and 69 mm inner diameter. Right, injector components : the air distributor in purple, the hollow cone fuel atomizer in orange, the swirler in green and the end plate in brown color. This plate features a conical converging hole having a 14 mm diameter inlet and an 8 mm diameter outlet. Adapted from [52, 53].

Table 2: Operating parameters for experiments using SnO_2 seeding in SICCA-Spray. Three slightly different configurations are used in this article. l_c is the length of the quartz confinement chamber, ϕ the global equivalence ratio of the combustible mixture, $\dot{m}_{C_7H_{16}}$ the fuel mass flow rate, u_b the bulk velocity at the outlet of the injector: $u_b = \dot{m}/(\pi\rho_{cold}r_{inj}^2)$, with $\dot{m}$ the air mass flow rate, ρ_{cold} the density of the unburnt mixture and r_{inj} the radius of the injector outlet. Concerning the imaging apparatus, $\mathcal{P}_{LASER}$ designates the power of the continuous 532 nm laser, the high speed camera can be equipped with two different lenses, with different apertures f_{lens}. The sampling frequency of the camera is noted f_s, and the exposure time δt.

Section	3	4	5
l_c(mm)	200	200	300
ϕ	0.87	0.95	0.95
$\dot{m}_{C_7H_{16}}$(g h^{-1})	400	440	440
u_b(m s^{-1})	32	32	32
$\mathcal{P}_{LASER}$(W)	10	15	15
Lens	25 mm	60 mm	60 mm
f_{lens}	f:0.95	f:2.8 (axial) or f:4 (normal)	
f_s(kHz)	100	40	40
δt(µs)	8.38	12.5	12.5
Resolution	384×264	512×512	512×512

3. Application to a highly swirled spray flame

3.1. Experimental set up

The SICCA-Spray swirled burner is used in this article (see [52, 54, 55] for more details on this experimental rig). It is displayed in Fig. 3, on the left. A quartz tube, open to the atmosphere, forms the combustion chamber. The tube has an inner diameter of 69 mm and its length l_c, alongside other experimental parameters, is reported in Tab. 2. The injector placed in this system is identical to that used in previous investigations on light round ignition in the MICCA-Spray annular chamber [2, 4, 21]. Components that make up this unit are shown on the right of Fig. 3. The fuel atomizer forms a hollow cone spray of liquid heptane on the axis of the burner. The mean Sauter diameter in the droplet spray d_{32} equals 27 µm [2]. A swirler, marked in teal in Fig. 3, sets the air in rotation around the axis. This swirler consists of 6 holes tangentially connected to the annular space surrounding the atomizer. The diameter of each hole is 3 mm and the distance between two axes of parallel holes is 10 mm. An end plate, with a converging conical hole, blocks the swirler in its housing. The central hole forming the outlet has a diameter of 8 mm. This results in a swirl number experimentally determined immediately downstream of the injector of 0.68 [2]. Two driver units are plugged on the system to modulate the flame by means of harmonic waves but they are not operated in the present study.

In the present article, three different experimental configurations have been investigated, and are detailed in Tab. 2. Note that the bulk velocity and air flow rates are kept constant for all three experimental configurations. The first operating conditions, used in the present section, match those of previous experiments and LES [2, 4, 21]. In section 4, the operating conditions are slightly richer and transient PVC dynamics are examined in conditions where the system is thermoacoustically stable. In section 5, the air and fuel flow rates are identical to Sec. 4, but a longer combustion chamber is used and a combustion oscillation, coupled by a longitudinal acoustic mode, occurs.

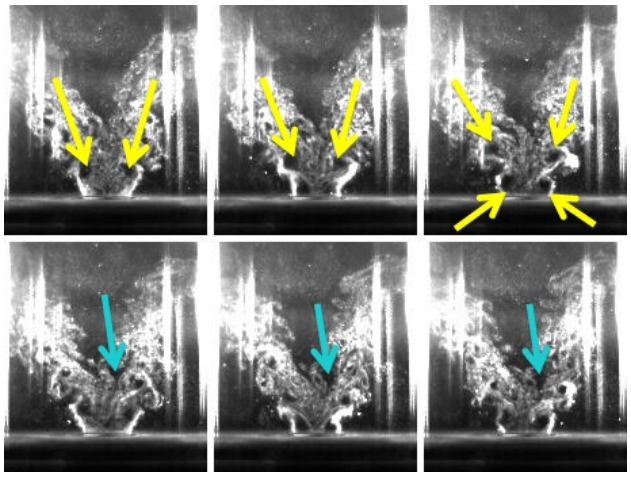

Figure 4: Successive flame images with SnO_2 seeding and illumination by a vertical laser sheet. The sequence is read from left to right and from top to bottom. Compared to the recorded sequence only one image out of 5 is displayed, which corresponds to a rate of 20 000 fps. Yellow arrows indicate the low pressure regions corresponding to the branches of the PVC. Blue arrows indicate the lower edge of the flame in the inner recirculation zone.

As in section 2 the flow is investigated using planar laser imaging. The laser sheet traverses the burner perpendicular to the axis or parallel to the axis along a diameter. The emission optics for the laser sheet is the same as in Section 2, with a laser sheet height of approximately 50 mm. The flow is seeded with tin dioxide micronic particles which quickly vanish at the temperatures reached with a heptane-air flame near stoichiometry. The dynamics of the flame front is visualized with a Photron FASTCAM SA-X2 high speed camera at a frame rate of 100,000 fps with an exposure time of $\delta t = 8.38\,\mu s$ for each image. At this frame rate, one may hope to capture the flame front motion and distinguish hot regions where temperatures are higher than 1770 K from cooler regions. The images displayed in Figs. 4 and 5 only show one image out of 5 selected from complete sequences to exhibit the dynamics of flow structures, therefore at an effective sampling rate corresponding to 20 kHz.

3.2. Swirling flame front dynamics

Axial (vertical) planar laser visualization are displayed in Fig. 4. Near the combustion chamber backplane, in the lower corners of the images, there are no SnO_2 particles indicating that these areas are occupied by recirculating burnt gases that are hot. On each side of the injector outlet the images are quite bright, because of the light scattered by the spray of heptane droplets that are shed from the periphery of the outlet hole (for images showing the extent of the spray in SICCA-Spray, see [55] (non reactive conditions) or [54] (reactive, unstable conditions)). Downstream, on the axis, one observes a large triangular area that is quite dark, indicating that tin dioxide particles are absent. This is an area filled with burnt gases recirculating towards the low pressure region formed around the centerline by the swirling flow. In each image in the second line, the lowest point of this region is indicated by a blue arrow. The flame penetrates deeply in the neighborhood of the central axis but the flame edge is also found to move downstream to a distance of 20 mm from the combustor backplane.

The external boundary of the spray and tin dioxide particles, near the injector outlet, sometimes features undulations induced by the vortices generated at the injector lip. The frequency of these vortices is high, but does not cause a specific flame motion. One distinguishes in these images dark areas that are symmetrical with respect to the axis of the burner and marked by yellow arrows in Fig. 4. They correspond to locations without particles that are surrounded by seeded areas. The absence of particles may be interpreted by considering that these dark areas correspond to a strong vortex from which particles are centrifuged. It is known that swirling flows may give rise to hydrodynamic instabilities taking the form of narrow and intense helical vortices with a precessing motion around the injector axis (PVC). If there is a single helix PVC ($m = 1$) the planar laser visualization would reveal unseeded spots with an alternate arrangement with respect to the central axis [30]. In the present case, however, the spots are symmetrical indicating that this could be due to the presence of two helical structures that are diametrically opposed (PVC with an azimuthal wavenumber $m = 2$) [25].

To see if this is indeed the case it is logical to observe what is happening in the normal (horizontal) direction. This may be done by placing a laser sheet parallel to the backplane at a distance $z = 5$ mm from the outlet (Fig. 5). The corresponding images show two opposite dark spots that rotate around the injector axis in the clockwise direction. These spots are marked with yellow arrows. One deduces from the horizontal and vertical visualizations that the flow features two helical structures nested one inside the other. This double helix configuration ($m = 2$) is less common than the single core PVC ($m = 1$) but is manifested in swirling flows characterized by high rotation rates as can be seen for example in [25] where the instantaneous vorticity field in a non-reactive flow with a high level of swirl features a double helix structure. The images presented in [25]

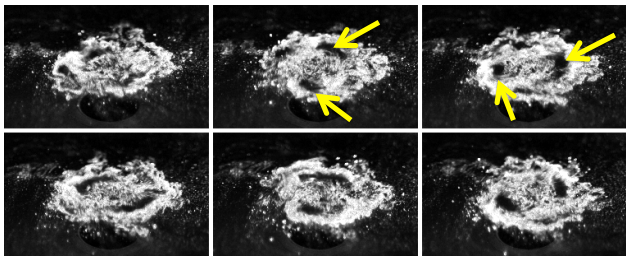

Figure 5: Successive flame images with SnO_2 seeding and illumination by a horizontal laser sheet, at z = 5 mm from the injector outlet. Photographs are taken with a high elevation angle of approximately 45°. The sequence is read from left to right, then from top to bottom. Compared to the recorded sequence only one image out of 5 is displayed, which corresponds to a rate of 20 000 fps. The yellow arrows indicate the low pressure regions corresponding to the arms of the two helicoidal cores.

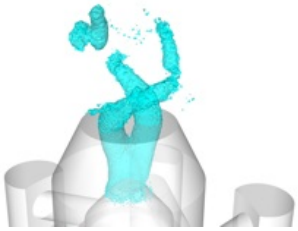

Figure 6: Large eddy simulation of the flow inside and at the outlet of the swirling injector. A pressure isosurface corresponding to 99 400 Pa is displayed showing the winding of the two helicoidal PVCs.

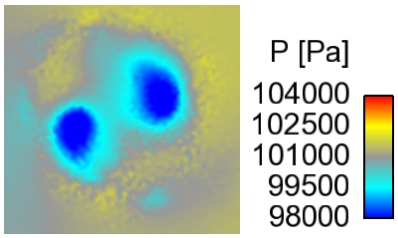

(a) Pressure

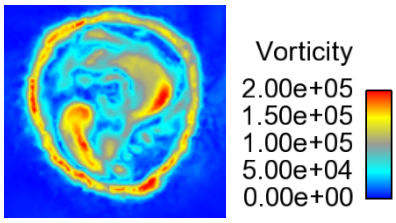

(b) Vorticity

Figure 7: (a) Instantaneous pressure field in a plane located at z = 1 mm above the injector outlet. (b) Instantaneous vorticity field in the same section. Values are given in s^{-1}. Two spots of low pressure and high vorticity are visible, and correspond to the intersection of the two PVC helicoidal structures with the viewing plane.

Table 3: Calculation of the Stokes number Stk_ω for tin dioxide particles in air in the presence of a vorticity of $2.0\,10^5 s^{-1}$.

$d(\mu m)$	0.39	1.04	1.37	2.86
$\tau_b(\mu s)$	3.23	22.9	39.8	174
Stk_ω	0.64	4.6	8.0	35

are strikingly similar to those displayed in Fig. 4.

Using the images of Fig. 5, it is possible to determine the precession frequency of each arm. This is found to be of 3.25 kHz corresponding to a Strouhal number St = $2R_{inj}f/u_b$ = 0.81, which falls in the typical range reported in [23].

To understand the origin of the deficits in tin dioxide particles in areas where the temperature is normally low, it is natural to seek an estimate of the vorticity level in these low pressure regions. This however would require measurements of the velocity field which is difficult to measure with PIV because the particles are absent from high vorticity regions. To get an estimate of the vorticity level one may use large eddy simulations of the same flow. The calculations carried out in [21] give access to this information. Results corresponding to conditions selected for the experiments appear in Fig. 6 which shows details of the injector geometry and an isosurface of the pressure field that materializes the helicoidal winding of the two vortex cores.

One may clearly see in Fig. 7(a) two low pressure regions corresponding to slices through the two PVCs wound as a double helix. In Fig. 7(b), the vorticity field in this same plane shows that the levels of vorticity reach of the order of $2.0\,10^5\,s^{-1}$. It is then possible to know if particles are circulating in the vortex by examining their Stokes number Stk_ω in this region. This number can be defined by $Stk_\omega = \tau_b/\tau_\omega$, where τ_ω is a characteristic residence time of a particle in the vortex and τ_b is the classical momentum relaxation time for particles featuring a low Reynolds number

$$\tau_b = \frac{\rho_b d_b^2}{18\mu_f} \tag{4}$$

where ρ_b, d_b are the particle density and diameter and μ_f designates the dynamical viscosity in the surrounding gaseous stream.

The characteristic residence time in a vortex featuring a vorticity level ω is inversely proportional to this level: $\tau_\omega \simeq \omega^{-1}$ [56, 57]. This can be used to estimate the Stokes number Stk_ω for tin dioxide particles in places where the vorticity level reaches maximum values. Results gathered in Tab. 3 indicate that the finest particles

have a Stokes number smaller than unity. They can theoretically follow the flow inside the vortex. However, the number of these small particles is relatively small (less than 10% of the total number of particles), their light scattering cross section is also small so that they will only contribute in a minor way to the light intensity measured by the camera. The particles having a diameter of the order of magnitude of one micron already have a Stokes number that is larger than 1, indicating that these particles will be centrifugated by the vortex structure. Thus more than 90% of the population will leave the zone where the vorticity is of $2.0\,10^5\,\mathrm{s}^{-1}$. It is therefore normal to observe a deficit of tin dioxide particles in the vortex core. This lack of particles is obviously inconvenient for velocity measurements in these areas, but it has the advantage of allowing the spatial localization of strong vortical structures such as a PVC.

4. PVC dynamics during intermittent flame flashbacks

4.1. POD based image processing

It is now interesting to implement a processing method for the analysis of the dynamics of the flame and PVCs. The present method features two steps: first, a Proper Orthogonal Decomposition is applied to the images. This statistical processing consists in expanding the images $\psi(x, y, t)$ onto a series of M modes $\Psi(x, y)$ in the spatial domain.

$$\psi(x, y, t) \approx \overline{\psi}(x, y) + \sum_{k=1}^{M} a_k(t)\Psi_k(x, y) \tag{5}$$

where a_k are temporal coefficients corresponding to the projection of ψ onto the mode Ψ_k and $\overline{\psi}$ is the mean value of ψ. If the number of modes M is equal to the number of images on which the POD is performed, then Eq. (5) is exact. The basis formed by the modes Ψ_k is orthogonal. The POD process allows to isolate dominant spatial structures. Thresholding for improved brightness and contrast is the only pre-processing applied prior to the POD.

The second step of the processing consists in the spectral analysis of the coefficients $a_k(t)$. This is performed by first computing their power spectral density using Welch's periodogram method. This step is useful to identify the dominant frequency of a structure, but transient dynamics are hidden by this type of processing. In a second step, time-frequency analysis is performed by means of a continuous wavelet transform based on an analytical Morlet wavelet [58]. The conversion of the scale of the wavelet transform to a frequency is based on an approximation whereby the center frequency f_{CM} of the mother Morlet wavelet is divided by the scale a: $f = f_{CM}/a$. The temporal resolution of the continuous wavelet transform is evaluated as the width at half height of the scalogram of an impulse. At a given frequency f, it corresponds to $\delta t = 1.56/f$. Results of this processing are plotted in the form of a scalogram in time-frequency coordinates. The color scale indicates the squared magnitude of the continuous wavelet transform, which is akin to a power spectral density plotted as a function of time and frequency. Note that Yin and Stöhr [9] exploit a similar approach (multi-resolution POD (MRPOD)), to study, among other things, the state of the PVC in a bi-stable flame.

In the present section, the operating conditions of the burner are slightly modified to match those that will be used in Section 5 to investigate the flame dynamics during a combustion instability. All relevant experimental parameters are gathered in Tab. 2. Compared to Section 3, the fuel flow rate is increased by 10% while the air flow rate is kept constant, corresponding to a global equivalence ratio of 0.96, and a thermal power of 5.4 kW. The image acquisition rate is set at 40 kHz with an exposure time of 12.5 µs.

Figure 8 shows the results of the POD analysis performed on a normal (horizontal) slice similar to that presented in Fig. 5. The energy distribution of the POD modes (Fig. 8(a)) reveals two dominant modes displayed in Fig. 8(b). Their shape corresponds to a set of two opposing holes (the $m = 2$ PVC located in the inner shear layer between the inner recirculation zone and the swirling jet), surrounded by two periodic bean shapes in the outer shear layer. These outer structures are fully synchronized with the precessing motion and are reported in several previous studies carried out in non-reacting conditions [25, 26, 30]. The second mode is similar to the first mode, with a $\pi/4$ rad rotation. The power spectral density of the coefficients (Fig. 8(d)) shows that the POD coefficients are harmonic with a frequency of 7.5 kHz, corresponding to a precession frequency of 3.75 kHz for each arm. The temporal coefficients a_1^h and a_2^h, where the superscript h is used to denote the result of horizontal slices, form a set of circles in a Lissajous diagram (Fig. 8(c)), indicating that the two POD modes are highly correlated and in phase quadrature. These elements constitute the typical signature of a periodic, progressive rotating pattern extracted using POD. Given the shape and spectral signature associated with the pair of POD modes, one concludes that these two modes correspond to the double helix PVC shown in Fig. 6. For a detailed discussion on the reconstruction of a PVC using POD, which further substanti-

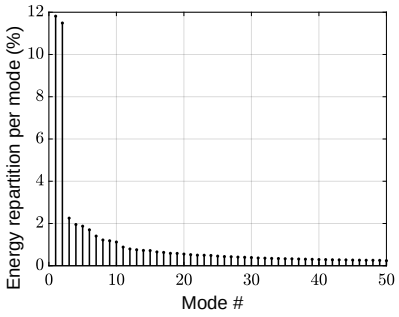

(a) Energy distribution in POD modes.

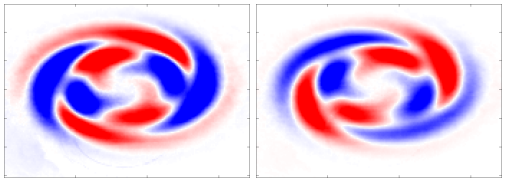

(b) POD modes 1 and 2.

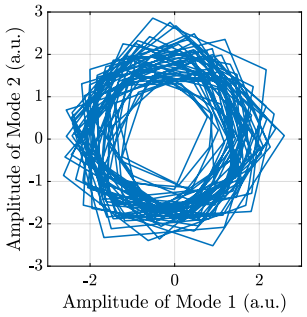

(c) $a_2^h(t)$, amplitude of POD mode 2, plotted against $a_1^h(t)$, amplitude of POD mode 1.

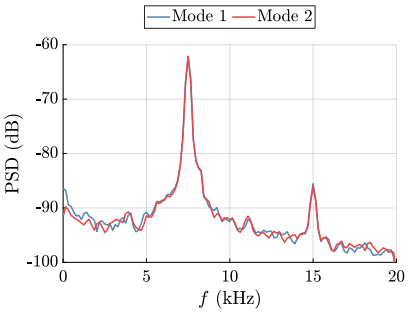

(d) Power spectral density of $a_1^h(t)$ and $a_2^h(t)$.

Figure 8: POD processing of images recorded with a horizontal laser sheet illumination at $z = 5$ mm above the backplane with a high viewing angle of approximately 45° with respect to the vertical direction. 5458 images are used for this processing.

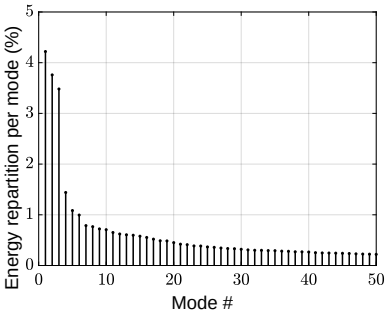

(a) Energy distribution in the POD modes.

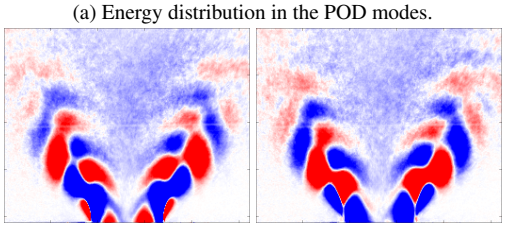

(b) POD modes 1 and 2.

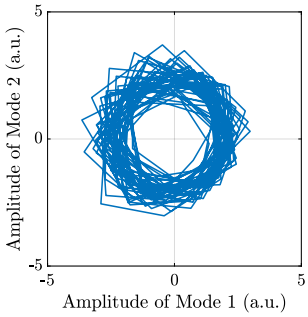

(c) $a_2^v(t)$, amplitude of POD mode 2, plotted against $a_1^v(t)$, amplitude of POD mode 1.

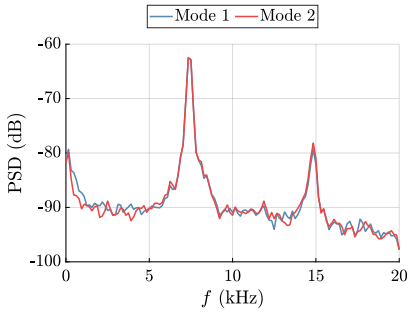

(d) Power spectral density of $a_1^v(t)$ and $a_2^v(t)$.

Figure 9: POD processing of particle images with vertical laser sheet illumination. 4366 images are used for this processing.

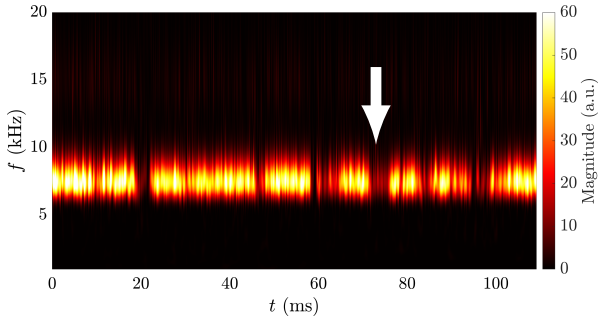

Figure 10: Scalogram of the POD coefficient $a_1^v(t)$, associated with the double helix, $m = 2$ PVC mode in the visualization with a vertical laser sheet illumination. Indicated by a white arrow is the gap in the scalogram that is studied in Section 4.2.

ate the elements that have been presented, one may refer to [30].

The same processing is now applied to images with illumination with an axial (vertical) laser sheet similar to those presented in Fig. 4, leading to the results shown in Fig. 9 which confirm the presence of two POD modes in quadrature. The first two modes that the POD exhibits also correspond to the double helix PVC. It is next interesting to perform a time-frequency analysis of this double helix PVC signal. This is done by making use of an analytical wavelet transform, performed on the $a_1^v(t)$ coefficient of the first POD mode from the vertical planar visualization. Figure 10 shows the resulting scalogram for a 110 ms recording. The frequency around 7.5 kHz is dominant, but one observes during certain short periods of time of a few milliseconds, that the signal corresponding to the double helix PVC vanishes. This intermittency manifests itself six times during the 110 ms long recording, and its duration varies between 2 ms and 7 ms. The intermittent disappearance of this double helix structure is studied in more detail in the next section.

4.2. *Changes in PVC regimes during intermittent flame flashbacks*

To analyze the intermittent gaps in the scalogram of Fig. 10, one may first examine the raw images in the time interval corresponding to one of these gaps. The focus is thus placed on the longest intermittency found in Fig. 10 between $t = 70$ and $t = 76.5$ ms. The images of Fig. 11 show the evolution of the flow during this period of time. Note that these images are not equally spaced in time. Keeping in mind that the tin dioxide particles vanish while crossing the flame front, and referring to the images of Fig. 4, one sees that in the images corresponding to $t = 70$ and $t = 76.5$ ms, the flame is "M"-shaped with an Inner Recirculation Zone (IRZ) filled with hot combustion products. This state of the flame is by far the most commonly observed during the 110 ms recording, but the images of Fig. 11 focus on a transient flame flashback phenomenon that happens intermittently. Note that in the present work, the term "flashback" is not used to designate a full flashback where the flame would propagate upstream up to the air plenum, but rather an event where the flame propagates in the IRZ and penetrates further upstream than the outlet of the injector. From $t = 70.5$ to $t = 72.3$ ms, only a very small number of tin dioxide particles is found in the IRZ. The leading point of the flame (blue arrows) is descending towards the outlet of the injection unit. From the first image, and approximately up to $t = 71.3$ ms, a symmetric trail of holes can be found on either side of the swirling jet of cold gases (yellow arrows). It corresponds to a vertical cut of the double helix PVC associated with the $m = 2$ azimuthal wavenumber. Between $t = 71.5$ and $t = 72.5$ ms, holes indicative of strong vortices are still present, but the pattern is asymmetric. The upstream motion of the hot gases in the IRZ has destroyed the $m = 2$ structure. At $t = 72.5$ ms, cold gases start to penetrate the IRZ which is filled with particles by $t = 73$ ms. This state is maintained more or less until $t = 76$ ms when hot gases start appearing inside the IRZ near the top of the image. At $t = 76.5$ ms, the flame returns to its nominal "M"-shape and one can again identify the symmetric trail of holes characteristic of the $m = 2$ PVC.

In order to examine the vortical structure associated with the PVC, the time-frequency analysis is now continued by performing another POD with images taken only during the instants bounding the flame flashback ($t = 70$ ms to $t = 78$ ms) and with a smaller region of interest focusing on the injector near-field. Results corresponding to the time sequence presented in Fig. 11 are shown in Fig. 12 for images with illumination from a vertical laser sheet. From top to bottom, the first mode (Fig. 12(a)) indicates the presence (negative $a_1^v(t)$ coefficient) or absence (positive $a_1^v(t)$ coefficient) of particles in the inner recirculation zone. From this mode and the images of Fig. 11, one may consider that a limited flashback occurs between $t = 70.5$ and $t = 72.5$ ms. The second mode (Fig. 12(b)) is similar to those displayed in Fig. 9, and correspond to a double helix ($m = 2$) PVC. One observes from the scalogram that its amplitude is small between $t = 71.5$ and $t = 76$ ms. The third and fourth POD modes of Fig. 12 correspond to structures in phase opposition on either side of the outlet of the injector. The frequency content of the third POD mode (Fig. 12(c)) is centered around 3.7 kHz, indicating that it corresponds to a first order ($m = 1$), single helix PVC.

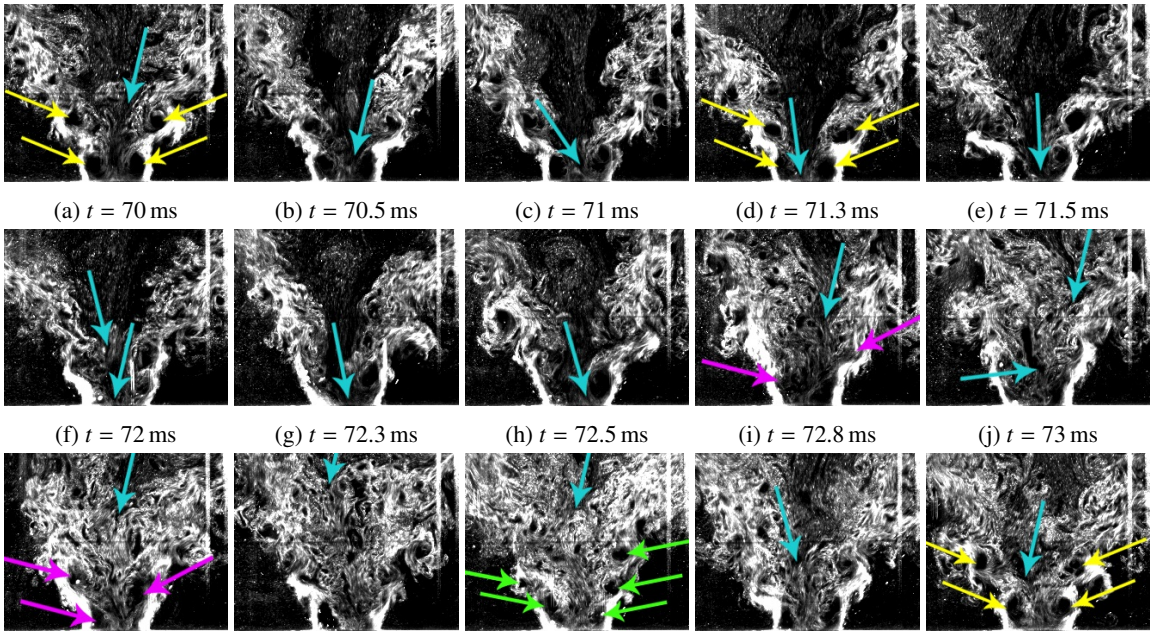

(a) $t = 70$ ms (b) $t = 70.5$ ms (c) $t = 71$ ms (d) $t = 71.3$ ms (e) $t = 71.5$ ms

(f) $t = 72$ ms (g) $t = 72.3$ ms (h) $t = 72.5$ ms (i) $t = 72.8$ ms (j) $t = 73$ ms

(k) $t = 73.4$ ms (l) $t = 74.5$ ms (m) $t = 75.5$ ms (n) $t = 76$ ms (o) $t = 76.5$ ms

Figure 11: Particle images with illumination by a vertical laser sheet. Images extracted between $t = 70$ and $t = 76.5$ ms. The sequence is arranged from left to right and from top to bottom. Note that the images are not equally spaced in time. The highly luminous regions on the side of the spray near the outlet of the injector can be associated with light scattered by the fuel droplets. Blue arrows indicate the location of the lowest position of the flame in the IRZ, and magenta (respectively yellow and green) arrows show areas devoid of seeding caused by a single (respectively double and triple) helix PVC. The interpretation of these raw Mie scattering images may be helped by also examining Fig. 14 for a better identification of the flame shape.

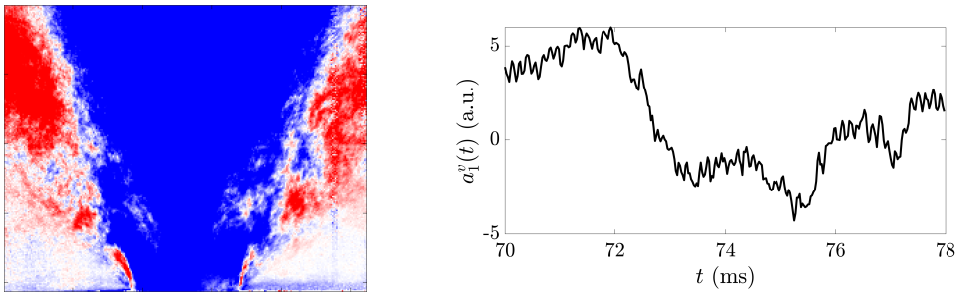

(a) POD mode associated with the presence of particles in the IRZ. A positive temporal coefficient $a_1^v(t)$ (graph on the right) indicates that the IRZ is devoid of particles, while a negative coefficient $a_1^v(t)$ corresponds to an IRZ filled with particles.

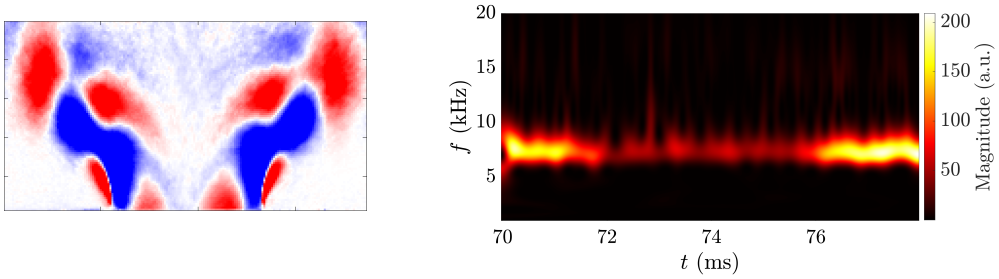

(b) POD mode associated with a double helix ($m = 2$) PVC. Its shape is symmetric and its frequency is 7.5 kHz.

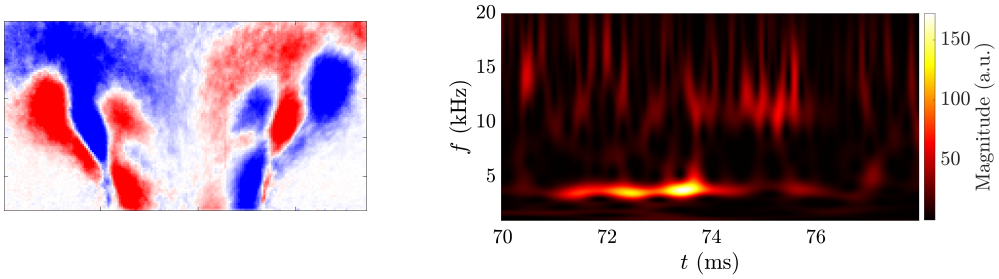

(c) POD mode associated with a single helix ($m = 1$) PVC. Its shape is asymmetric and its frequency is found around 3.7 kHz.

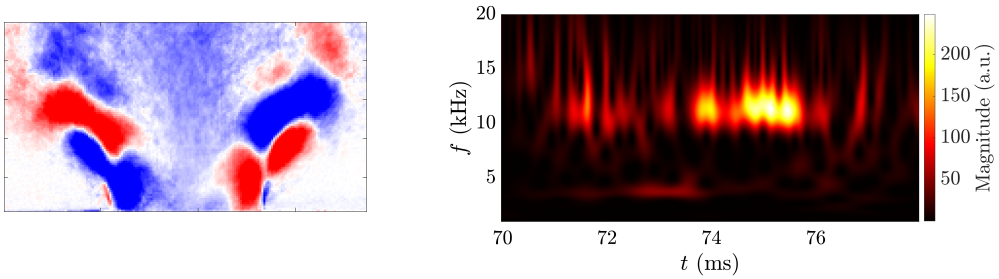

(d) POD mode associated with a triple helix ($m = 3$) PVC. It is characterized by its asymmetric structure and a frequency content centered around 11 kHz.

Figure 12: Spatial shape of the POD modes (left), and associated scalograms (right). The processing is performed between $t = 70$ and $t = 78$ ms, corresponding to the images of Fig. 11. **(a)** POD mode showing whether the IRZ is filled or devoid of particle during the flashback. **(b-d)** POD modes associated with coherent helical structures. Each structure is naturally associated to a pair of POD modes in quadrature with each other as in Fig. 9. Here, only one mode per structure is plotted for the sake of brevity.

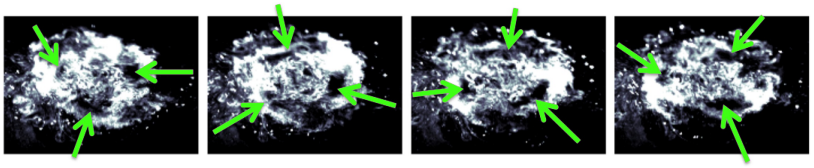

Figure 13: Horizontal slices illustrating a $m = 3$ PVC. These 4 selected images are separated by 25 µs.

It is present between $t = 71$ and $t = 74$ ms, and subsequently vanishes at $t = 74.7$ ms. The signature of this structure is also visible in Fig. 11 where it is marked by magenta arrows at $t = 72.8$ and $t = 73.4$ ms. Concerning the last mode (Fig. 12(d)), its frequency content is centered around 11 kHz, indicating that the POD modes pertain to a triple helix PVC ($m = 3$). This mode appear at $t = 73.7$ ms and is quite strong between $t = 74.5$ and $t = 75.8$ ms. Its signature can also be seen on the images of Fig. 11 at $t = 75.5$ ms among others: three holes are located on the right side of the jet, two on its left side, all indicated by green arrows. These holes are staggered, and the spacing between the holes is smaller than that observed with the $m = 2$ PVC holes (yellow arrows). This further confirms the interpretation of the POD and wavelet processing as the signature of a triple helix PVC during these instants. This structure can additionally be observed on horizontal slices from a separate recording and shown in Fig. 13. During a short time period, three holes rotating around the axis can also be distinguished.

The analysis presented in Fig. 12 is also performed on four other intermittent flashback events identified in Fig. 10, and on horizontal laser sheet visualization as well (two events), with similar results that are not included here for the sake of brevity. The analysis reveals that three states of the Precessing Vortex Core can exist in this system, and that these three states are linked to different stages in intermittent flashback events:

- The double helix PVC ($m = 2$) discussed in Section 3.2 is by far the most common structure in this flow, and is most often present.
- A PVC of azimuthal wavenumber $m = 1$ precessing at a frequency of 3.75 kHz can also be observed for short periods of time. This structure appears during intermittent flame flashbacks in the IRZ, while the flame and the IRZ penetrate inside the injection unit, and may be maintained for up to a millisecond after the end of flashback.
- A PVC of azimuthal wavenumber $m = 3$ appearing at a frequency of 11.1 kHz in the processed signal. This structure has the shape of three intertwined helices.

During seven intermittent flashback events that have been studied, the azimuthal wavenumber was always found to follow the sequence $m = 2$ followed by $m = 1$ and by $m = 3$, before returning to the steady state $m = 2$.

One may then try to explain these transitions from a theoretical viewpoint. It is known from recent stability analysis of the PVC (for example [27]) that the wavemaker region which controls the amplitude and growth rate of this structure is located slightly upstream of the vortex breakdown bubble. The same conclusion is reached in [59] using a structural linear analysis of a Turbomeca helicopter engine injector. These studies are mainly concerned with single helix ($m = 1$) PVCs. Contrary to the $m = 1$ PVC, the $m = 2$ mode has two wavemaker regions: one slightly upstream of the vortex breakdown bubble, and a second one further upstream [42]. It is also noted [39] that the PVC may be damped by changes in the velocity and density distributions. These elements suggest that the changes in the flow structure in the wavemaker region accompanying the intermittent flashback may induce damping of certain PVC modes and growth of others.

5. Analysis of flame and PVC dynamics during a combustion instability

An important research question concerns the fate of the PVC during strong acoustic oscillations in the flow. Recent work in reactive flows are reviewed in [24, 60] and in the introductions of [61, 62]. A first topic of interest is the energy transfer between the helical and acoustic modes. As the PVC is a helical instability, in perfectly axisymmetric flames, it does not directly feed acoustic energy into the thermoacoustic oscillation [38]. However, Acharya and Lieuwen [63] suggest that, if the flame is not perfectly axisymmetric, the helical mode might feed energy into a longitudinal acoustic mode. In the case of high frequency combustion instabilities driven by transverse acoustic modes (so called "screech"), Ghani et al. [33] indicate that the PVC can strongly interact with the acoustic field and drive the instability. In some experimental and LES studies, it is found that acoustic forcing suppresses the PVC

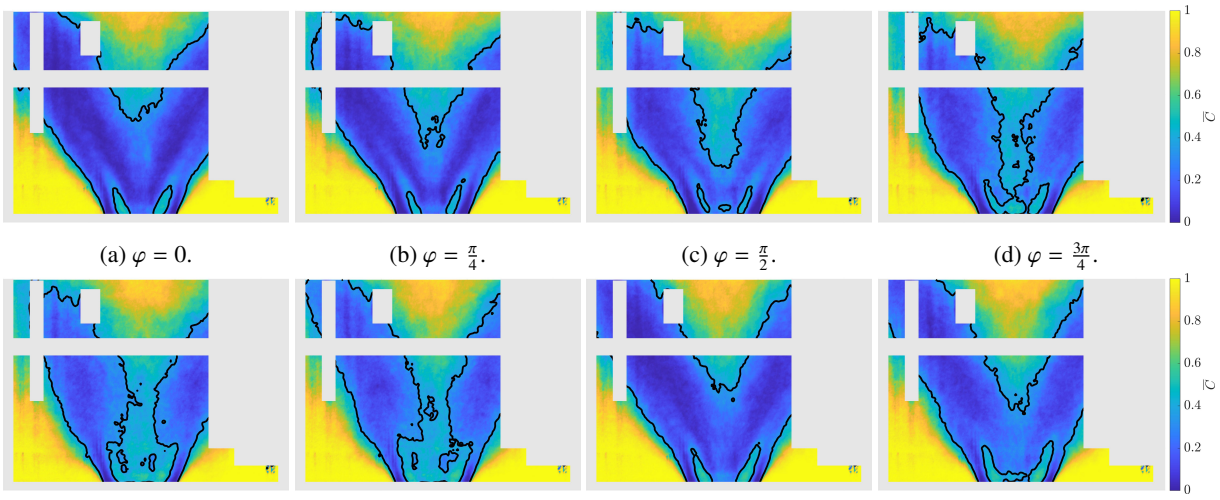

(a) $\varphi = 0$. (b) $\varphi = \frac{\pi}{4}$. (c) $\varphi = \frac{\pi}{2}$. (d) $\varphi = \frac{3\pi}{4}$.

(e) $\varphi = \pi$. (f) $\varphi = \frac{5\pi}{4}$. (g) $\varphi = \frac{3\pi}{2}$. (h) $\varphi = \frac{7\pi}{4}$.

Figure 14: **(a - h)** Estimate of the phase averaged progress variable $\overline{C}$. $\overline{C} \approx 0$ indicates a region with a high probability of observing SnO_2 particles, $\overline{C} \approx 1$ regions with a low probability of observing SnO_2 particles. A black isocontour at $\overline{C} = 0.35$ is added to the images. Some reflections of the laser sheet are visible on the images due to the cylindrical shape of the quartz tube. The largest ones are hidden by gray rectangles. Note that a bias is introduced in areas where the PVC is strong due to the absence of particles in the core of the vortex. Only the very bottom part of the images is affected by the PVC, on either side of the centerline.

[23, 38, 61, 64, 65]. In the study of Renaud et al. [62] carried out in a liquid-fueled burner, the PVC is not observed in the gaseous flow downstream of the injector but its presence can be detected as it perturbs the liquid fuel spray, and consequently, the flame. The perturbation caused by the PVC also vanishes under high forcing amplitudes. On the other hand, in some studies, the PVC is enhanced by the acoustic forcing [66]. In acoustically forced flows where a PVC can be detected, spectral analysis generally reveals a peak at $f_{PVC} - f_a$, the difference between the frequency of the PVC and that of the acoustic forcing [9, 38, 61, 62], indicating that the helical structure is modulated by the acoustic perturbation. One should note that, in the aforementioned studies, the acoustic frequency is often higher, or of the same order of magnitude as that of the PVC. Terhaar et al. [61] propose a classification of PVC-acoustic interaction, distinguishing between "mean flow correction", that is a change in the mean flow caused by acoustic fluctuations that subsequently modifies the PVC through the mechanisms presented in their previous study [39], and "mean flow modulation", where the PVC is modulated. They suggest that the latter scenario can be modeled using a parametrically forced oscillator.

This section is focused on the dynamics of the flame under the operating conditions defined previously (Section 4.1), but with a longer combustion chamber of total length $l_c = 300\,\text{mm}$. This gives rise to thermoacoustic oscillations at a frequency of 473 Hz, such that the frequency f_{PVC} of the PVC is approximately one order of magnitude larger than f_a, the frequency of the acoustic oscillation, a situation not commonly examined in the previous literature. Photomultiplier measurements of excited OH^* radical emission give an indication as to the level of unsteady heat release rate fluctuations. It reaches $I'_{OH^*}/\overline{I_{OH^*}} = 23.4\%$ (RMS).

The present section is organized as follows: firstly, phase-averaged tin dioxide images with planar laser illumination are used to examine the dynamics of the inner recirculation zone during the oscillation cycle (Sec. 5.1); then the dynamics of the PVC interacting with the thermoacoustic instability is examined (Sec. 5.2) and intermittency in the azimuthal wavenumber of the PVC is discussed (Sec. 5.3).

5.1. Dynamics of the inner recirculation zone

In order to investigate the dynamics of the inner recirculation zone during the combustion oscillation, slices obtained by illuminating the flow and flame seeded with micronic SnO_2 particles with a vertical laser sheet are acquired at a sampling rate of 40 kHz. The addition of SnO_2 microparticles does not significantly affect the flame as the mean value and amplitude of the PM signal remain unchanged. The images are then processed as follows: a Gaussian filter with a kernel size of 3×3 pixels and a standard deviation of 0.5 is first applied to

remove noise. The images are then binarized to distinguish regions where SnO_2 particles are present (fresh gases and laser reflections) and those where they have vanished (hot combustion products and strong vortices). The non-parametric method of Otsu [67] is used to determine the threshold. In this method, the threshold is independent of the exposure and seeder density in a particular image, which allows a reliable comparison between different configurations and phase instants. This method has been used with success in combustion applications to process particle, chemiluminescence and PLIF images [17, 68, 69]. Phase averaging is then performed with bins of $\pi/8$ rad. The reference signal for the phase averaging process is the temporal coefficient $a_1^v(t)$ of the first POD mode which mostly captures the flame motion related to the combustion oscillation.

Results are shown in Fig. 14 as a color map featuring the phase averaged progress variable $\overline{C}$. The inner recirculation zone oscillates during the cycle: between $-\pi/2 < \varphi < \pi/2$, the bottom of the recirculation zone of hot combustion products is located several injector outlet diameters above the backplane. Between $3\pi/4 < \varphi < 5\pi/4$, the leading edge of the flame in the inner recirculation zone is located much closer to the outlet of the injector and is indistinguishable from the area where the PVC is strong. In addition isocontours at $\overline{C} = 0.35$ are plotted for different phase instants in Fig. 15. The movement of the upper part of the flame is unfortunately mostly hidden by laser reflections. One may only faintly distinguish in the upper left corner that the tip of the flame is slightly longer for $5\pi/4 < \varphi < 2\pi$ than at other phase instants. On the other end, in the vicinity of the outer recirculation zone, all isocontours $\overline{C} = 0.35$ are clearly visible. They are superimposed, indicating that there is no lateral motion of the flame front.

5.2. *Analysis of the PVC modulated by a combustion instability*

The POD and wavelet based processing method used in Section 4.1 is now employed to analyze the same axial (vertical) slices acquired during combustion instability. Results presented in this section focus on the time-frequency analysis of one of the POD modes corresponding to a double helix PVC.

Figure 16 displays the results of the POD processing. Three POD modes contain most of the energy, and Fig. 16(a) shows the power spectral density of their temporal coefficients. Mode #1 corresponds to the motion of the flame caused by the combustion instability (hence its previous use as a reference for phase averaging). Its power spectral density has a strong peak

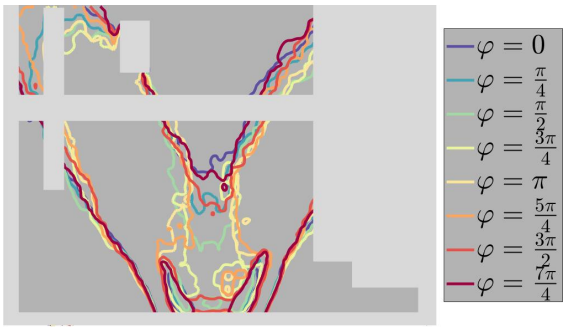

Figure 15: Isocontours at $\overline{C} = 0.35$ plotted for 8 phase instants. Some reflections of the laser sheet are visible on the images due to the cylindrical shape of the quartz tube. The largest ones are hidden with a lighter shade of gray. Note that a bias is introduced in areas where the PVC is strong due to the absence of particles in the core of the vortex. Only the very bottom part of the images is affected by the PVC, on either side of the centerline.

at the frequency of the oscillation (473 Hz). Modes #2 and #3 have a shape corresponding to a double helix ($m = 2$) PVC. Their frequency content is centered around 7.4 kHz. The shape of their power spectral density is however peculiar, with a valley at 7.4 kHz surrounded by several peaks. Carrying a wavelet-based time-frequency analysis on mode #2 allows to understand this shape. The scalogram of a_2^v (POD coefficient of mode #2, shown in Fig. 16(b)) shows a repetitive motive of "hat-like" patterns. The instantaneous frequency of a_2^v extracted from the scalogram (center frequency associated with the scale at which the coefficient is largest at a given instant, shown in Fig. 16(c)) oscillates between approximately 6.3 and 8.4 kHz. Similarly, the instantaneous amplitude of a_2^v (largest coefficient of the scalogram at a given instant, shown in Fig. 16(d)) also oscillates at the frequency of the instability. The modulation of the PVC can be further characterized by calculating the power spectral densities of the instantaneous frequency $f_{\#2}$ and amplitude A_2^v extracted from the wavelet analysis (not shown here). Both of these power spectral densities are characterized by a prominent peak at 468 Hz, the frequency of the combustion oscillation. One may then conclude that the PVC is modulated by the combustion oscillation, both in frequency and in amplitude.

In SICCA-Spray, the very large difference in frequency between the acoustic mode and the precessing frequency of the PVC allows to clearly identify the mean flow modulation effect on the helical structure that was proposed by Terhaar et al. [61]. However, their theoretical model based on a parametrically forced oscillator predicts that acoustic forcing at a very small fre-

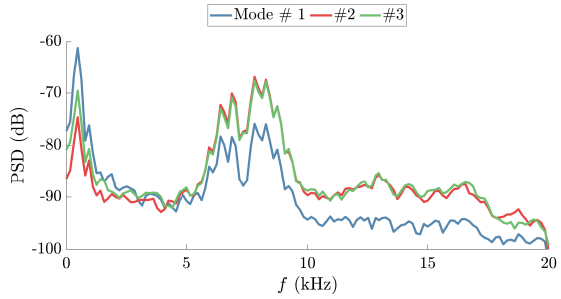

(a) Power spectral density of a_1^v, a_2^v and a_3^v.

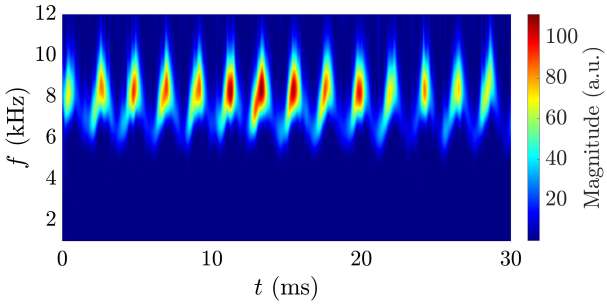

(b) Scalogram of POD mode # 2.

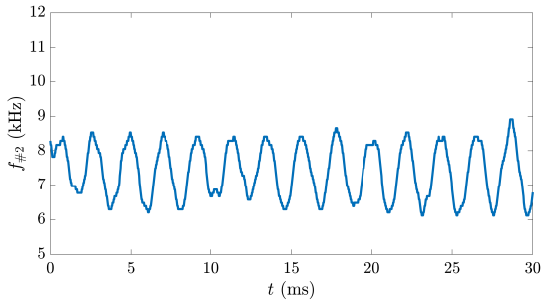

(c) Instantaneous frequency of POD mode # 2 (from wavelet analysis).

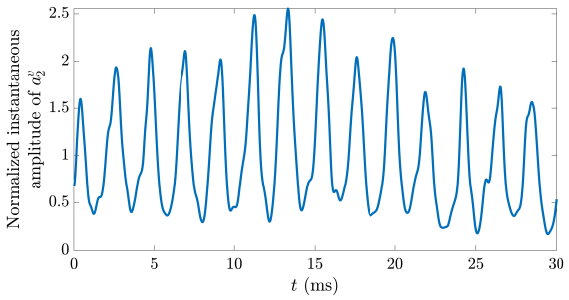

(d) Instantaneous amplitude of POD mode # 2 (from wavelet analysis). The instantaneous amplitude is normalized by the mean amplitude of a_2^v.

Figure 16: Time-frequency analysis of POD mode of vertical tin dioxide planar laser illumination images taken during a combustion instability. The focus is mainly placed on POD mode # 2, associated with a double helix PVC. The POD processing was performed on 4366 images.

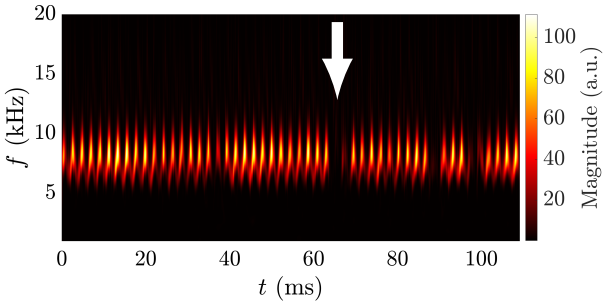

Figure 17: Scalogram of POD coefficient $a_2^v(t)$, associated with the double helix, $m = 2$ PVC mode in the vertical slices during a combustion oscillation. Indicated by a white arrow is a gap in the scalogram.

quency ($10 f_a \approx f_{PVC}$) would result in the complete destruction of the helical structure. This is not observed in the present configuration.

In numerous experiments reviewed by [23] and conducted without acoustic forcing, the frequency of the PVC has been found to be linearly correlated with the injector bulk velocity. This corresponds to a constant value of the Strouhal number $\mathrm{St} = 2R_{inj}f/u_b$. During the combustion instability studied in the present section, the frequency of the PVC is modulated with a peak-to-peak amplitude of 2.2 kHz. Under a quasi-stationary hypothesis, one may then tentatively estimate that the amplitude of fluctuation of the injector bulk velocity is in the order of $u_b'/\overline{u}_b \approx 11\%$ RMS.

5.3. PVC intermittency during a combustion oscillation

Figure 17 is similar to Fig. 16(b): it shows the scalogram of the POD coefficient $a_2^v(t)$ associated with the $m = 2$ wavenumber PVC, but over a longer time duration. It presents gaps. The same analysis as that conducted in Fig. 10 (not detailed here for the sake of brevity) shows that the gaps occur in a similar manner during combustion oscillations and in thermoacoustically stable conditions: at the beginning of the gaps, the inner recirculation of hot combustion products penetrates deeper within the injection unit, and this leads to the disappearance of the $m = 2$ PVC. Then, a single helix structure with an azimuthal wavenumber $m = 1$ is observed, followed by a return to the usual $m = 2$ structure. However, the helical structure of azimuthal wavenumber $m = 3$ is never observed during the combustion oscillation.

Another important difference between thermoacoustically stable and unstable operation is the duration of the gaps. In Fig. 17, the gaps appear to have a duration corresponding to one or two acoustic periods. The histogram of gap durations normalized by the acoustic

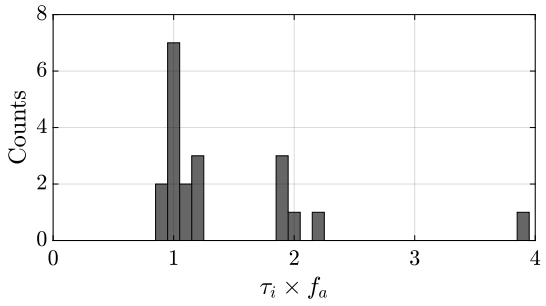

Figure 18: Histogram showing the duration τ_i of gaps in the signal associated with the $m = 2$ PVC. The duration of the gap is normalized by the acoustic period. Statistics are gathered over several recordings for a total of 20 events. To determine τ_i, the instantaneous amplitude of the POD coefficient a_2^v is processed using the peak finding algorithm of Matlab to calculate the width at half prominence of peaks corresponding to the gaps.

period (Fig. 18) shows that these gaps have a duration that is a multiple of the acoustic period, indicating that the thermoacoustic oscillation is able to lock the state of the PVC for one or more acoustic periods.

6. Conclusion

This article explores a high repetition rate flame imaging method using tin dioxide particles and its application to a strongly swirled spray flame. These particles are interesting as flow tracers because the temperature at which they vanish is much higher than that of the oil droplets commonly used to locate flame fronts in combustion studies. It is shown that these particles when seeded in the flow and illuminated by a laser sheet give access to structural features in the flow and can be used to determine the structure and dynamics of flame fronts under conditions where the temperature of the gases feeding the flame is already high and would lead to the vaporization of many other types of tracers like oil droplets.

The first part of this study is aimed at specifying the temperature T_v at which the tin dioxide particles vanish. This is accomplished by means of a methane-air stagnation point flame configuration. Experiments in combination with calculations yield a value of approximately $T_v = 1770\,\mathrm{K}$ for the disappearance temperature. This indicates that the particles vanish by the chemical reaction $SnO_2(s) + CO(g) \rightleftharpoons SnO(g) + CO_2(g)$ in hydrocarbon-air flames.

The flow is then seeded with tin oxide particles and illuminated by a planar laser sheet to identify precessing vortex cores formed by a swirled injector and to study the dynamics of flames formed by this injector. High speed visualization at 100 kHz reveal the presence of a double helicoidal structure. Although this structure dominates the flow, a time frequency-analysis based on POD reveals a more complex behavior. Intermittent flame flashback, during which the flame and the IRZ penetrate into the injector, randomly occur during steady operation of the burner. During these events, the double helix PVC is damped and vanishes to leave place to a single helix structure. This state of the flow is not stable, and fresh gases subsequently fill the inner recirculation zone. At these instants, the PVC features a triple helix structure. The flow and flame then return to their normal state with a double helix PVC.

This novel experimental method in combination with time-frequency-analysis is finally used to study the dynamics of the PVC during a combustion instability characterized by an acoustic frequency an order of magnitude smaller than the frequency of the PVC. Phase averaged images of SnO_2 laser illuminated slices reveal the dynamics of the inner recirculation zone during the combustion oscillation and indicate that the leading edge of the flame in the IRZ has a strong axial motion during the thermoacoustic cycle. It is also found that the double helix PVC is the dominant PVC mode. The large difference in frequency between the PVC and the acoustic forcing allows the determination of the instantaneous frequency and amplitude of the PVC and shows that it is modulated, both in amplitude and in frequency. The modulation frequency is that of the thermoacoustic oscillation. The oscillating mass flow rate at the outlet of the injector is most likely the cause of the modulation of the PVC. Limited flashback events into the IRZ are also observed during the combustion instability and lead to changes in the azimuthal wavenumber of the PVC.

Acknowledgments

The authors wish to thank CERFACS and IFPen for sharing the AVBP solver. This work is supported by the French Agence Nationale de la Recherche (grant FASMIC ANR16-CE22-0013 and TIMBER ANR14-CE23-0009-01). Access to HPC resources was granted by the “Mésocentre” computing center of CentraleSupélec and École Normale Supérieure Paris-Saclay supported by CNRS and Région Île-de-France. This work was also granted access to the HPC resources of TGCC and IDRIS under the allocation 2017-A0022B10118 attributed by GENCI (Grand Equipement National de Calcul Intensif). Useful discussion with Dr. Kevin Prieur are gratefully acknowledged.

[1] A.-M. Kypraiou, N. A. Worth, E. Mastorakos, Experimental Investigation of the Response of Premixed and Non-premixed Tur-

bulent Flames to Acoustic Forcing, in: 54th AIAA Aerospace Sciences Meeting, American Institute of Aeronautics and Astronautics, Reston, Virginia, 2016.

[2] K. Prieur, D. Durox, J. Beaunier, T. Schuller, S. Candel, Ignition dynamics in an annular combustor for liquid spray and premixed gaseous injection, Proceedings of the Combustion Institute 36 (3) (2017) 3717–3724.

[3] D. Ebi, N. T. Clemens, Simultaneous high-speed 3D flame front detection and tomographic PIV, Measurement Science and Technology 27 (3) (2016) 035303.

[4] K. Prieur, G. Vignat, D. Durox, T. Schuller, S. Candel, Flame and spray dynamics during the light-round process in an annular system equipped with multiple swirl spray injectors, Journal of Engineering for Gas Turbines and Power 141 (6) 061007.

[5] F. Greiffenhagen, J. Woisetschläger, J. Gürtler, J. Czarske, Quantitative measurement of density fluctuations with a full-field laser interferometric vibrometer, Experiments in Fluids 61 (1) (2020) 1–15.

[6] D. E. Cavaliere, J. Kariuki, E. Mastorakos, A comparison of the blow-off behaviour of swirl-stabilized premixed, non-premixed and spray flames, Flow, Turbulence and Combustion 91 (2) (2013) 347–372.

[7] J. R. Osborne, S. A. Ramji, C. D. Carter, A. M. Steinberg, Relationship between local reaction rate and flame structure in turbulent premixed flames from simultaneous 10 kHz TPIV, OH PLIF, and CH2O PLIF, Proceedings of the Combustion Institute 36 (2) (2017) 1835–1841.

[8] M. Stöhr, K. Oberleithner, M. Sieber, Z. Yin, W. Meier, Experimental Study of Transient Mechanisms of Bistable Flame Shape Transitions in a Swirl Combustor, Journal of Engineering for Gas Turbines and Power 140 (1) (2018) 011503.

[9] Z. Yin, M. Stöhr, Time-frequency localisation of intermittent dynamics in a bistable turbulent swirl flame, Journal of Fluid Mechanics 882 (2020) A301–A3042.

[10] L. Boyer, Laser tomographic method for flame front movement studies, Combustion and Flame 39 (3) (1980) 321–323.

[11] D. Durox, S. Ducruix, Concerning the Location of the Schlieren Limit in Premixed Flames, Combustion and Flame 120 (2000) 595–598.

[12] J.-P. Dumont, R. Borghi, A Qualitative Study by Laser Tomography of the Structure of Turbulent Flames, Combustion Science and Technology 48 (3-4) (1986) 107–128.

[13] P. C. Miles, F. C. Gouldin, Premixed turbulent flame/flow interaction: Simultaneous measurements of velocity and flamelet position, AIAA Journal 36 (7) (1998) 1178–1189.

[14] J. R. Hertzberg, M. Namazian, L. Talbot, A laser tomographic study of a laminar flame in a Karman vortex street, Combustion Science and Technology 38 (3-4) (1984) 205–216.

[15] M. Mouqallid, B. Lecordier, M. Trinite, High Speed Laser Tomography Analysis of Flame Propagation in a Simulated Internal Combustion Engine - Applications to Nonuniform Mixture, in: SAE Technical Paper, 1994, p. 941990.

[16] B. Lecordier, M. Mouqallid, S. Vottier, E. Rouland, D. Allano, M. Trinite, CCD Recording method for cross-correlation PIV development in unstationary high speed flow, Experiments in Fluids 17 (3) (1994) 205–208.

[17] S. Balusamy, A. Cessou, B. Lecordier, Direct measurement of local instantaneous laminar burning velocity by a new PIV algorithm, Experiments in Fluids 50 (4) (2011) 1109–1121.

[18] T. D. Upton, D. D. Verhoeven, D. E. Hudgins, High-resolution computed tomography of a turbulent reacting flow, Experiments in Fluids 50 (1) (2011) 125–134.

[19] L.-D. Chen, W. Roquemore, Visualization of jet flames, Combustion and Flame 66 (1) (1986) 81–86.

[20] Pubchem, tin(iv) oxide.
URL https://pubchem.ncbi.nlm.nih.gov/compound/29011

[21] T. Lancien, K. Prieur, D. Durox, S. Candel, R. Vicquelin, Large Eddy Simulation of Light Round in an Annular Combustor with Liquid Spray Injection and Comparison with Experiments, Journal of Engineering for Gas Turbines and Power 140 (2) (2018) 021504.

[22] O. Lucca-Negro, T. O'Doherty, Vortex breakdown: A review, Progress in Energy and Combustion Science 27 (4) (2001) 431–481.

[23] N. Syred, A review of oscillation mechanisms and the role of the precessing vortex core (PVC) in swirl combustion systems, Progress in Energy and Combustion Science 32 (2) (2006) 93–161.

[24] S. Candel, D. Durox, T. Schuller, J.-F. Bourgouin, J. P. Moeck, Dynamics of Swirling Flames, Annual Review of Fluid Mechanics 46 (2014) 147–73.

[25] H. Liang, T. Maxworthy, An experimental investigation of swirling jets, Journal of Fluid Mechanics 525 (2005) 115–159.

[26] K. Oberleithner, M. Sieber, C. N. Nayeri, C. O. Paschereit, C. Petz, H.-C. Hege, B. R. Noack, I. Wygnanski, Three-dimensional coherent structures in a swirling jet undergoing vortex breakdown: Stability analysis and empirical mode construction, Journal of Fluid Mechanics 679 (2011) 383–414.

[27] K. Manoharan, M. Frederick, S. Clees, J. O'Connor, S. Hemchandra, A weakly nonlinear analysis of the precessing vortex core oscillation in a variable swirl turbulent round jet, Journal of Fluid Mechanics 884 (2020) A29.

[28] L. Selle, G. Lartigue, T. Poinsot, R. Koch, K. U. Schildmacher, W. Krebs, B. Prade, P. Kaufmann, D. Veynante, Compressible large eddy simulation of turbulent combustion in complex geometry on unstructured meshes, Combustion and Flame 137 (4) (2004) 489–505.

[29] S. Wang, S. Y. Hsieh, V. Yang, Unsteady flow evolution in swirl injector with radial entry. I. Stationary conditions, Physics of Fluids 17 (4) (2005) 045106.

[30] M. Stöhr, R. Sadanandan, W. Meier, Phase-resolved characterization of vortex-flame interaction in a turbulent swirl flame, Experiments in Fluids 51 (4) (2011) 1153–1167.

[31] F. Gallaire, M. Ruith, E. Meiburg, J.-M. Chomaz, P. Huerre, Spiral vortex breakdown as a global mode, Journal of Fluid Mechanics 549 (2006) 71–80.

[32] S. Wang, Z. Rusak, R. Gong, F. Liu, On the three-dimensional stability of a solid-body rotation flow in a finite-length rotating pipe, Journal of Fluid Mechanics 797 (2017) 284–321.

[33] A. Ghani, T. Poinsot, L. Gicquel, J. D. Müller, LES Study of Transverse Acoustic Instabilities in a Swirled Kerosene/Air Combustion Chamber, Flow, Turbulence and Combustion 96 (1) (2016) 207–226.

[34] J. J. Cassidy, H. T. Falvey, Observations of unsteady flow arising after vortex breakdown, Journal of Fluid Mechanics 41 (4) (1970) 727–736.

[35] D. Froud, T. O'Doherty, N. Syred, Phase averaging of the precessing vortex core in a swirl burner under piloted and premixed combustion conditions, Combustion and Flame 100 (3) (1995) 2–11.

[36] S. Roux, G. Lartigue, T. Poinsot, U. Meier, C. Bérat, Studies of mean and unsteady flow in a swirled combustor using experiments, acoustic analysis, and large eddy simulations, Combustion and Flame 141 (1-2) (2005) 40–54.

[37] G. Kuenne, A. Ketelheun, J. Janicka, LES modeling of premixed combustion using a thickened flame approach coupled with FGM tabulated chemistry, Combustion and Flame 158 (9) (2011) 1750–1767.

[38] J. P. Moeck, J.-F. Bourgouin, D. Durox, T. Schuller, S. Candel, Nonlinear interaction between a precessing vortex core and

acoustic oscillations in a turbulent swirling flame, Combustion and Flame 159 (8) (2012) 2650–2668.
[39] S. Terhaar, K. Oberleithner, C. O. Paschereit, Key parameters governing the precessing vortex core in reacting flows: An experimental and analytical study, Proceedings of the Combustion Institute 35 (3) (2015) 3347–3354.
[40] K. Rajamanickam, S. Basu, Insights into the dynamics of conical breakdown modes in coaxial swirling flow field, Journal of Fluid Mechanics 853 (2018) 72–110.
[41] P. Billant, J.-M. Chomaz, P. Huerre, Experimental study of vortex breakdown in swirling jets, Journal of Fluid Mechanics 376 (1998) 183–219.
[42] M. Vanierschot, J. S. Müller, M. Sieber, M. Percin, B. W. van Oudheusden, K. Oberleithner, Single- and double-helix vortex breakdown as twodominant global modes in turbulent swirlingjetflow, Journal of Fluid Mechanics 883 (2020) A31.
[43] M. O. Vigueras-Zuñiga, A. Valera-Medina, N. Syred, Studies of the precessing vortex core in swirling flows, Journal of Applied Research and Technology 10 (5) (2012) 755–765.
[44] D. Froud, A. Beale, T. O'Doherty, N. Syred, Studies of Helmholtz resonance in a swirl/furnace system, Symposium (International) on Combustion 26 (2) (1996) 3355–3362.
[45] N. Syred, J. M. Beer, Damping of precessing vortex cores by combustion in swirl generators, Astronautica Acta 17 (4-5) (1972) 783–801.
[46] G. P. Smith, D. M. Golden, M. Frenklach, N. W. Moriarty, B. Eiteneer, M. Goldenberg, T. C. Bowman, R. K. Hanson, S. Song, W. C. J. Gardiner, V. V. Lissianski, Z. Qin, http://www.me.berkeley.edu/gri_mech/.
[47] R. H. Lamoreaux, D. L. Hildenbrand, L. Brewer, High-Temperature Vaporization Behavior of Oxides II. Oxides of Be, Mg, Ca, Sr, Ba, B, Al, Ga, In, Tl, Si, Ge, Sn, Pb, Zn, Cd, and Hg, Journal of Physical and Chemical Reference Data 16 (3) (1987) 419–443.
[48] K. Schofield, Trace species reported combustion behavior and their chemistry, in: Combustion Emissions, 2020, pp. 23–467.
[49] Z. Galazka, R. Uecker, D. Klimm, K. Irmscher, M. Pietsch, R. Schewski, M. Albrecht, A. Kwasniewski, S. Ganschow, D. Schulz, C. Guguschev, R. Bertram, M. Bickermann, R. Fornari, Growth, characterization, and properties of bulk SnO2 single crystals, Physica Status Solidi (A) Applications and Materials Science 211 (1) (2014) 66–73.
[50] J. A. Marley, T. C. MacAvoy, Growth of Stannic Oxide Crystals from the Vapor Phase, Journal of Applied Physics 32 (12) (1961) 2504–2505.
[51] C. L. Hoenig, A. W. Searcy, Knudsen and Langmuir Evaporation Studies of Stannic Oxide, Journal of the American Ceramic Society 49 (3) (1966) 128–134.
[52] G. Vignat, D. Durox, K. Prieur, S. Candel, An experimental study into the effect of injector pressure loss on self-sustained combustion instabilities in a swirled spray burner, Proceedings of the Combustion Institute 37 (4) (2019) 5205–5213.
[53] G. Vignat, D. Durox, A. Renaud, S. Candel, High Amplitude Combustion Instabilities in an Annular Combustor Inducing Pressure Field Deformation and Flame Blow Off, Journal of Engineering for Gas Turbine and Power 142 (1) (2020) 011016.
[54] G. Vignat, E. Lo Schiavo, D. Laera, A. Renaud, L. Gicquel, D. Durox, S. Candel, Dynamics of spray and swirling flame under acoustic oscillations: A joint experimental and LES investigation, Proceedings of the Combustion Institute 000 (2020) 1–10. doi:10.1016/j.proci.2020.05.054.
[55] G. Vignat, P. Rajendram Soundararajan, D. Durox, A. Vié, A. Renaud, S. Candel, A joint experimental and LES characterization of the liquid fuel spray in a swirl injector, in: Proceedings of ASME Turbo Expo, 2020, pp. GT2020–14935.
[56] A. R. Kriebel, Particle Trajectories in a Gas Centrifuge, Journal of Basic Engineering 83 (3) (1961) 333.
[57] R. P. Dring, M. Suo, Particle trajectories in swirling flows, Journal of Energy 2 (4) (1978) 232–237.
[58] N. Delprat, P. Guillemain, B. Escudie, R. Kronland-Martinet, P. Tchamitchian, B. Torresani, Asymptotic Wavelet and Gabor Analysis: Extraction of Instantaneous Frequencies, IEEE Transactions on Information Theory 38 (2) (1992) 644–664.
[59] O. Tammisola, M. P. Juniper, Coherent structures in a swirl injector at Re = 4800 by nonlinear simulations and linear global modes, Journal of Fluid Mechanics 792 (2016) 620–657.
[60] Y. Huang, V. Yang, Dynamics and stability of lean-premixed swirl-stabilized combustion, Progress in Energy and Combustion Science 35 (4) (2009) 293–364.
[61] S. Terhaar, B. Ćosić, C. O. Paschereit, K. Oberleithner, Suppression and excitation of the precessing vortex core by acoustic velocity fluctuations: An experimental and analytical study, Combustion and Flame 172 (2016) 234–251.
[62] A. Renaud, S. Ducruix, L. Zimmer, Experimental Study of the Precessing Vortex Core Impact on the Liquid Fuel Spray in a Gas Turbine Model Combustor, Journal of Engineering for Gas Turbines and Power 141 (11) (2019) 111022.
[63] V. Acharya, T. Lieuwen, Nonlinear response of swirling premixed flames to helical flow disturbances, Journal of Fluid Mechanics 896 (2020) A6.
[64] P. Iudiciani, C. Duwig, Large eddy simulation of the sensitivity of vortex breakdown and flame stabilisation to axial forcing, Flow, Turbulence and Combustion 86 (3-4) (2011) 639–666.
[65] S. V. Alekseenko, V. M. Dulin, Y. S. Kozorezov, D. M. Markovich, Effect of high-amplitude forcing on turbulent combustion intensity and vortex core precession in a strongly swirling lifted propane/air flame, Combustion Science and Technology 184 (10-11) (2012) 1862–1890.
[66] A. Giauque, L. Selle, L. Gicquel, T. Poinsot, H. Buechner, P. Kaufmann, W. Krebs, System identification of a large-scale swirled partially premixed combustor using LES and measurements, Journal of Turbulence 6 (2005) N21.
[67] N. Otsu, Threshold selection method for gray level histograms, IEEE Transactions on Systems, Man and Cybernetics SMC-9 (1) (1979) 62–66.
[68] A. Degenève, R. Vicquelin, C. Mirat, B. Labegorre, P. Jourdaine, J. Caudal, T. Schuller, Scaling relations for the length of coaxial oxy-flames with and without swirl, Proceedings of the Combustion Institute 37 (4) (2019) 4563–4570.
[69] N. Rock, B. Emerson, J. Seitzman, T. Lieuwen, Near-lean blowoff dynamics in a liquid fueled combustor, Combustion and Flame 212 (2020) 53–66.